Title:

Two-Photon AMPK and ATP Imaging Reveals Metabolic Recovery in Mouse Rod Photoreceptor Cells.

Abbreviated title:

Two-photon imaging of photoreceptor metabolism.

Jiazhou He[1], Masamichi Yamamoto[2], Kenta Sumiyama[3], Yumi Konagaya[1,a], Kenta Terai[1],

Michiyuki Matsuda[1,4,5], and Shinya Sato[1,b]

[1]Laboratory of Bioimaging and Cell Signaling, Graduate School of Biostudies, Kyoto University, Kyoto 606-8501, Japan.

[2]Department of Research Promotion and Management, National Cerebral and Cardiovascular Center, Research Institute, Osaka 565-8565, Japan.

[3]Laboratory for Mouse Genetic Engineering, RIKEN Center for Biosystems Dynamics Research, Osaka, 565-0871, Japan.

[4]Department of Pathology and Biology of Diseases, Graduate School of Medicine, Kyoto University, Kyoto 606-8501, Japan.

[5]Institute for Integrated Cell-Material Sciences, Kyoto University, Kyoto 606-8501, Japan.

[a]Present address: Department of Cell and Developmental Biology, Weill Cornell Medicine, 1300 York Ave, New York, NY, 10065, USA.

[b]Present address: Department of Advanced Medical Technologies, National Cerebral and Cardiovascular Center, Research Institute, Suita, Osaka 565-8565, Japan.

Correspondence: Shinya Sato, Department of Advanced Medical Technologies, National Cerebral and

Cardiovascular Center Research Institute, 6-1 Kishibe-Shinmachi, Suita, Osaka 565-8565, Japan.

E-mail: sato.shinya@ncvc.go.jp

Nonstandard abbreviations: RPE, retinal pigmented epithelium; OXPHOS, oxidative phosphorylation; AMPK, AMP-activated protein kinase; 2-DG, 2-deoxy-D-glucose; ERG, electroretinogram; B6J, C57BL/6J; DMEM/F12, Dulbecco's modified Eagle's medium/nutrient mixture F-12 Ham; PNA, peanut agglutinin; GaAsP, gallium arsenide phosphide; FRET, Förster resonance energy transfer; GCL, ganglion cell layer; IPL, inner plexiform layer; INL, inner nuclear layer; OPL, outer plexiform layer; ONL, outer nuclear layer; PRS, photoreceptor segments; CRALBP, cellular retinaldehyde-binding protein; AICAR, 5-aminoimidazole-4-carboxamide-1-β-D-ribofuranoside; GRK1, G-protein receptor kinase 1; GC, guanylate cyclase.

Conflict of interest statement: The authors declare no conflicts of interest.

Author contributions: S. Sato and M. Matsuda designed the research; J. He, Y. Konagaya and S. Sato performed the experiments; K. Sumiyama produced transgenic mice; M. Yamamoto provided transgenic mice; J. He and S. Sato analyzed data and wrote the manuscript; Y. Konagaya, K. Terai and M. Matsuda edited the manuscript.

Abstract

In vertebrates, retinal rod and cone photoreceptor cells rely significantly on glycolysis. Lactate released from photoreceptor cells fuels neighboring retinal pigmented epithelium (RPE) cells and Müller glial cells through oxidative phosphorylation (OXPHOS). To understand this highly heterogeneous metabolic environment around photoreceptor cells, single-cell analysis is needed. Here, we visualized cellular AMP-activated protein kinase (AMPK) activity and ATP levels in the retina by two-photon microscopy. Transgenic mice expressing a hyBRET-AMPK biosensor were used for measuring the AMPK activity. GO-ATeam2 transgenic mice were used for measuring the ATP level. Temporal metabolic responses were successfully detected in the live retinal explants upon drug perfusion. A glycolysis inhibitor, 2-deoxy-D-glucose (2-DG), activated AMPK and reduced ATP. These effects were clearly stronger in rods than in cones. Notably, rod AMPK and ATP started to recover at 30 min from the onset of 2-DG perfusion. Consistent with these findings, *ex vivo* electroretinogram (ERG) recordings showed a transient slowdown in rod dim flash responses during a 60-min 2-DG perfusion, whereas cone responses were not affected. Based on these results, we propose that cones surrounded by highly glycolytic rods become less dependent on glycolysis, and rods also become less dependent on glycolysis within 60 min upon the glycolysis inhibition.

Introduction

Rod and cone photoreceptor cells in the vertebrate retina consume ATP at very high rates (1, 2). However, these cells are strongly reliant on glycolysis (3-5), which produces only 2 ATP molecules from one glucose in contrast to the theoretically 38 ATPs generated in mitochondrial oxidative phosphorylation (OXPHOS). In photoreceptor cells, more than 80% of glucose is converted to lactate through glycolysis even in the presence of oxygen (3, 6). This aerobic glycolysis supplies metabolic intermediates for a daily 10% self-renewal of the photoreceptor outer segment (7), a membrane-rich organelle embedded with ~5 mM of rhodopsin (8). The light detection efficacy of the outer segment is 5–10 times higher at the newly synthesized base than at the spent tip (9). Therefore, glycolysis supports the outer segment biogenesis to maintain highly light-sensitive rod-mediated vision.

Photoreceptor cells form symbiotic relationships with surrounding cells to process metabolites. Lactate released from photoreceptor cells fuels the surrounding retinal pigmented epithelium (RPE) cells and Müller glial cells (10). In this system, the relationship between the neurons and glia is the opposite of that in the common astrocyte-neuron lactate shuttle hypothesis, which posits that lactate is produced from astroglia and used in neurons (5). Other models of the metabolic interdependence between photoreceptor cells and RPE cells have been proposed recently: a malate-succinate shuttle model (11), a model of phagocytosis-dependent ketogenesis in the RPE (12), and a proline-mediated metabolic communication model (13). These mechanisms, collectively called the metabolic ecosystem or metabolic landscape of the retina (4, 5), suggest the importance of symbiotic metabolic programs for the integrity of photoreceptor cells.

Many studies have addressed the metabolic differences between rods and cones. Calculated ATP consumption is clearly larger in cones than in rods in mice, mainly because cones make more synapses (2). In addition, microscopic analyses showed that cones contain more mitochondrial mass than rods (14-16). Consistent with these reports, a recent metabolomics analysis detected more significant pyruvate consumption in the cone-rich retinal samples than in their rod-rich counterparts (17). Chronic glycolysis inhibition by cone-specific hexokinase-2 knockout did not change cone electroretinogram (ERG) responses or mitochondrial mass, whereas rod-specific knockout changed both (18). These lines of evidence support that cones depend more on

4

OXPHOS than rods to produce ATP efficiently. However, the cone-dominant ground squirrel retina uses about 95% of glucose through glycolysis (19). To reconcile these findings, a side-by-side comparison of rod and cone metabolism in the same tissue by live-imaging is needed.

Here, we visualized the AMP-activated protein kinase (AMPK) activity and ATP level in the mouse retina by two-photon microscopy. AMPK is a heterotrimeric protein kinase which is activated under low ATP and high AMP conditions to support energy-producing processes (20). Retinal explants prepared from hyBRET-AMPK (21) and GO-ATeam2 (22) transgenic mice were used in the AMPK and ATP imaging, respectively. Our live imaging successfully detected metabolic responses in the retina upon delivery of common AMPK activators and resolved the different responses in rods and cones.

Materials and Methods

Ethical approval

The animal protocols were reviewed and approved by the Animal Care and Use Committee of Kyoto University Graduate School of Medicine (MedKyo17539, 17539-2, 18086, 19090, and 20081) and methods were carried out in accordance with the relevant guidelines and regulations.

Reagents

PCR reagents and primers were obtained from Takara Bio (Kusatsu, Shiga, Japan) and Fasmac (Atsugi, Kanagawa, Japan), respectively. Catalog numbers and suppliers of other reagents are listed in Table S1.

Plasmid construction

To construct a biosensor for the AMPK activity, a DNA fragment coding the region from the sensor domain to the ligand domain in the pT2ADW-hyBRET-ERK plasmid (23) was replaced with that from AMPKAR-EV (21), to obtain the pT2ADW-hyBRET-AMPK plasmid.

Animals

hyBRET-AMPK transgenic mice were generated by Tol2-mediated gene transfer (24) using the pT2ADW-hyBRET-AMPK plasmid. Founder animals were bred with B6N-Tyr^{c-Brd}/BrdCrCr mice (B6 albino; Charles River Laboratories Japan, Yokohama, Kanagawa, Japan) for more than five generations to establish a stable line named hyBRET-AMPK (nbio327; NIBIOHN, Ibaraki, Osaka, Japan). This albino hyBRET-AMPK mouse was further bred with a normal pigmented C57BL/6J (B6J) mouse for more than 5 generations, and the resulting mice were maintained as heterozygous and used for experiments. GO-ATeam2 mice (22) were maintained as homozygous mice by inbreeding. The background strain is B6J. Rod transducin alpha-subunit knockout mice (*Gnat1*$^{-/-}$, B6J background) (25) were kindly provided by Dr. Vladimir J. Kefalov.

Preparation of the retinal explant and perfusion system for live imaging

The retinal explant and perfusion system was prepared according to a method described in our recent paper (26) with slight modifications, as detailed in the Supplemental Information. For the cone labeling in Figure 3, the isolated retina was incubated in Dulbecco's modified Eagle's medium/nutrient mixture F-12 Ham (DMEM/F12) supplemented with PNA-Alexa prior to the flat-mounting procedure. For the hyBRET-AMPK mouse, the retina was incubated with 10 µg/mL PNA-Alexa568 throughout the 15-min dissection procedure. For the GO-ATeam2 mouse, the retina was incubated with 10 µg/mL PNA-Alexa594 for 1 h in a 6-well-plate supplied with a humidified O_2/CO_2 gas mixture (Figure S1). The explant was washed in 5 mL DMEM/F12 for 2 min and used for imaging.

Two-photon microscopy for live imaging

Retina were observed with either an upright multi-photon microscope FV1000MPE-BX61 (Olympus, Tokyo, Japan), equipped with four multialkali detectors and a Ti:sapphire laser (tunable range 690–1040 nm; Mai-tai DeepSee HP; Spectra-Physics, Santa Clara, CA, USA) or an upright multi-photon microscope FV1200MPE-BX61, equipped with two GaAsP detectors, two multialkali detectors, a 1040 nm laser, and a tunable laser (680–1300 nm; InSight DeepSee; Spectra-Physics). A water immersion objective lens (XLPLN25XWMP; Olympus) was used in all experiments. The excitation laser wavelength was tuned at 840 nm for hyBRET-AMPK and 930 nm for GO-ATeam2 imaging. The fluorescent signal was split with the dichroic mirrors and filters shown in Table 1 and detected with multialkali or GaAsP detectors. Images were acquired with FV10-ASW software (Olympus).

Image processing and analysis

Images were processed on Fiji (image J version 1.53; https://fiji.sc). Detailed procedures were described in the ImageJ macro format and deposited in the SSBD:repository (https://doi.org/10.24631/ssbd.repos.2021.05.003). Briefly, the background signal was experimentally determined for each channel as a mean intensity in the blank

7

image and subtracted from retinal images. The positional drift was corrected with the Correct 3D drift plug-in (27). Longitudinal view (XZ view) images were reconstructed from Z-stack images. Multiple slices or frames were averaged to reduce noise. Pseudo-color AMPK or ATP images were created by multiplying 8-color FRET/CFP or FRET/GFP images with the corresponding grayscale images. For the rod-cone comparison in Figure 3, cone areas were segmented based on the positions of the PNA-Alexa signal.

In Figure 3D–F, the leak of the Alexa594 signal into the FRET Ch (Figure S2A) was subtracted using an experimentally determined leak factor. A non-fluorescent wild type B6J retina was incubated with PNA-Alexa594 and imaged in the same manner as the GO-ATeam2 retina (Figure S2B). The intensity ratio between FRET Ch and Alexa594 Ch was used as the leak factor (Figure S2C).

In Figure 3, the time-lapse image data that showed a >50% fluorescent intensity reduction were omitted from the analysis because the rod-cone segmentation did not appear to be accurate when the intensity of the PNA-Alexa signals was limited.

The parameters in Table 2 were obtained by fitting. The rising phase of the drug response was fitted with the following exponential curve function:

$$R = R_{max} \cdot \left(1 - e^{\frac{(D-t)}{\tau}}\right) + C$$

where R_{max} is the maximum amplitude of the response, t is the time, D is the delay of the response, τ is the time constant, and C is the basal AMPK activity.

ex vivo ERG

The *ex vivo* ERG was performed using a previously described method (28, 29) with modifications. Details are provided in the Supplemental Information. The acrylic retina holder (Figure S3A) was fabricated in the machine shop of Kyoto University. A pair of electrodes were made from the parts depicted in Figure S3B. DMEM/F12 supplemented with 1% (v/v) penicillin streptomycin mixture, 100 µM barium chloride, and 40 µM DL-2-amino-4-phosphonobutyric acid was used for perfusion to isolate the photoreceptor ERG component (30).

Mice were kept in a dark box for >3 h, typically overnight, before the experiments. Rod recordings were

obtained from B6J wild type retinas. Cone recordings were obtained from *Gnat1*^{-/-} retinas. The mouse was anesthetized by isoflurane inhalation for 1 min and immediately killed by cervical dislocation. The retinas were isolated in DMEM/F12, put on the acrylic retina holder, and perfused at 1 mL/min. Photoresponses were elicited with ~2 ms flashes of light. The LED light source device is described in our previous paper (26). The stimulation and recording were synchronized on Labchart Pro 8 software (ADInstruments; Dunedin, Otago, New Zealand). The light intensity was adjusted by a combination of ND filters (#48-090, #48-092, #48-093, and #36-273; Edmund Optics, Barrington, NJ, USA) in the LED device and a calibrated input voltage applied to the LED. A 500 nm bandpass filter (#88-300; Edmund Optics) was used for all stimulations in this study. The light was delivered through a liquid light guide (LLG03-4H; Thorlabs, Newton, NJ, USA) and projected on the retina as a circular light spot 3 mm in diameter (Figure S3C). The light intensity was calibrated with an optical power meter (TQ8210; Advantest, Tokyo, Japan). The flash duration was calibrated with a phototransistor (NJL7205L; New Japan Radio, Tokyo, Japan). Photoresponse data were analyzed on Clampfit 10.7 (Molecular Devices, San Jose, CA, USA). The data were digitally low-pass filtered at 30 Hz for noise reduction.

Results

Biosensors were expressed ubiquitously in hyBRET-AMPK and GO-ATeam2 retinas.

First, we characterized the distributions of the biosensors in the isolated retinas from hyBRET-AMPK and GO-ATeam2 mice. A retinal explant was flat-mounted on a culture insert with the ganglion cell-side up, perfused with DMEM/F12 culture medium, and imaged using a two-photon microscope. Fluorescent signals were detected throughout the retina at single cell resolution (Figure 1). The nuclear-sparing pattern in the hyBRET-AMPK retina (Figure 1A, B) is ascribed to the nuclear export signal peptide in the biosensor (23). The longitudinal view of the retina (Figure 1B) was reconstructed from the Z-stack data. Normal 9–10 rows of nuclei were detected in the outer nuclear layer (ONL), indicating that the photoreceptor survival was not compromised by the biosensor expression. Similar results were obtained from the GO-ATeam2 retina (Figure 1C, D). A group of nuclei in the inner nuclear layer (INL) showed fluorescence, probably because the GO-ATeam2 biosensor was not added with the localization signal peptide (31).

In both the hyBRET-AMPK and GO-ATeam2 retinas, a subset of cells in the ganglion cell layer (GCL) and inner plexiform layer (IPL) showed higher fluorescent signals than the other cells. These highly fluorescent cells show inverted triangle morphology in the GCL, which coincides with the endfeet of Müller glial cells. As expected, immunohistochemistry using an antibody to cellular retinaldehyde-binding protein (CRALBP), a molecular marker of the Müller cells, showed labeling on the highly fluorescent cells (Figure S4), indicating that the highly fluorescent cells were Müller cells. In a future study, this characteristic distribution would allow us to contrast the metabolic regulation of glial cells and neurons.

AMPK activity and ATP level were perturbed differently by three AMPK activators.

Next, we validated the response of the hyBRET-AMPK biosensor in the retina. A hyBRET-AMPK biosensor was created by inserting the sensor and ligand domains of the original AMPK sensor, AMPKAR-EV, into the hyBRET backbone (23). The function of the AMPKAR-EV was previously validated in culture cells using three common AMPK activators, 2-deoxy-D-glucose (2-DG), 5-aminoimidazole-4-carboxamide-1-β-D-

ribofuranoside (AICAR), and metformin (21). Here, these three drugs were used to confirm the function of the hyBRET-AMPK biosensor. The hyBRET-AMPK retina was time-lapse imaged and delivered with each AMPK activator during the indicated time window (Figure 2A). Although the time required to the plateau differed among the activators (Figure 2B), significant increases were detected with all three activators throughout the retina including GCL, IPL and photoreceptor segments (PRS) (Figure 2C). Therefore, we concluded that hyBRET-AMPK biosensor is functional.

Interestingly, the temporal patterns of the AMPK activation differed among the three drugs and among retinal layers. For quantitative comparison of these patterns, each response was fitted with an exponential curve to estimate the amplitude and time constant (Table 2). 2-DG activation of AMPK was about ten times faster, and the level of AMPK activation was about three times greater, in the PRS than in the other layers (Figure 2B, left). Notably, the activity in the PRS started to decline within 30 min even in the presence of 2-DG. In contrast, AICAR activated AMPK in the PRS about three times slower than in the other layers (Figure 2B, center). Metformin activated AMPK 2–70 times slower than the other two activators (Figure 2B, right).

The function of the GO-ATeam2 biosensor has already been validated (31). Here, we examined the effects of the three AMPK activators on the ATP level using GO-ATeam2 retinas (Figure 2D–F). 2-DG reduced the ATP level in the retina. We further noticed that the ATP level decreased more robustly in the IPL and PRS than the GCL. In correspondence with the AMPK result, the ATP level started to recover from after 30 min only in the PRS (Figure 2E, left). AICAR had only marginal effects on the ATP level (Figure 2E, F, center). Interestingly, metformin increased the ATP level slowly (Figure 2E, right), and the ATP level began to decrease only in the IPL at 100 min.

Taken together, these findings validated the function of the hyBRET-AMPK biosensor and visualized spatiotemporally characteristic responses of the retinal AMPK and ATP to the three AMPK activators. Among these responses, we discovered photoreceptor-specific recovery in the AMPK activity (Figure 2B) and ATP level (Figure 2E) from the midpoint of the 2-DG delivery. We were interested in examining whether the rods and cones would show different responses to 2-DG. Next, therefore, we further characterized the effects of 2-

11

DG in photoreceptor cells.

Rods showed larger 2-DG-induced AMPK and ATP responses than cones.

To distinguish rods and cones, the hyBRET-AMPK retinal explant was incubated with PNA-Alexa568, which

has affinity for the cone sheath (32). As expected, PNA-Alexa568 showed doughnut-like staining at the PRS

plane (Figure 3A, PNA-Alexa568). These PNA-positive areas were used to delineate cones from rods (Figure

3A, dashed circles). We found that rods exhibited more robust response than cones (Figure 3B). The initial

activation in rods was two times larger than that in cones, and the subsequent recovery in rods was three times

larger than that in cones (Figure 3C). During the following 60 min washout period, both the rod and cone

AMPK activities reverted to the baseline level.

To identify cones in the GO-ATeam2 retina, PNA-Alexa594 was used in order to minimize the spectral

overlap (Figure S2A); however, the bleedthrough of the Alexa594 fluorescence into the FRET channel was still

not negligible. Therefore, the bleedthrough was subtracted by using the experimentally determined leak factor

(see Materials and Methods and Figure S2B, C). Consistent with the AMPK response to 2-DG, rods exhibited

larger response to 2-DG than cones, followed by a complete recovery during the 60 min washout period (Figure

3D, E). The initial drop in rods was two times larger than in cones, and the subsequent recovery in rods was

four times larger than that in cones (Figure 3F). Together, these observations indicate that rods are more

sensitive to the 2-DG-induced glycolysis inhibition than cones. It is also noteworthy that rods can partially

restore the ATP level through a mechanism that responds as early as 30 min from the onset of the inhibition.

2-DG transiently slowed down the dim flash response specifically in rods.

To examine the impact of 2-DG on the electrophysiological performance of rods and cones, dim flash responses

were recorded by the *ex vivo* ERG (28). Although imaging data were obtained from the light-adapted retinas,

ERG responses were recorded from the dark-adapted retinas. Therefore, prior to the ERG analysis, we

confirmed that 2-DG induces AMPK and ATP responses similarly in light- or dark-adapted retinal specimens (Figure 4A).

First, rod ERG responses were recorded from wild type (WT) retinas. The photoreceptor component was isolated using the blocker cocktail as described previously (30). Dim flash responses were periodically recorded for 70 min. In the control recordings, the response amplitude declined gradually, while the response waveform did not change (Figure 4B, C, WT rod control). Quantitative analysis using the integration time supported that the response waveform did not change significantly (Figure 4D, Rod control). In the recordings with 2-DG, overall, the decline in amplitude was similar to that in the control (Figure 4B, C, WT rod 2-DG). In contrast, the response waveform widened significantly upon the 2-DG perfusion and reverted in 60 min. Similar to the recovery in the rod AMPK activity and ATP level (Figure 3), the integration time of the response showed rapid increase followed by gradual recovery during the 60 min 2-DG perfusion (Figure 4D, Rod 2-DG).

Next, dim flash responses of cones were recorded from $Gnat1^{-/-}$ retinas (28). Cone responses were elicited by 1000 photons μm^{-2} flashes that is 100 times stronger than that in the rod recordings. In contrast to the rod response, the cone response was not affected by 2-DG in either amplitude or waveform (Figure 4B–D, $Gnat1^{-/-}$ cone 2-DG). This observation agrees with the moderate responses in the AMPK activity and ATP level in cones (Figure 3).

Finally, to test whether AMPK activation is sufficient to slow down the rod response, the same analysis was performed in the presence of AICAR (Figure 4B, WT Rod AICAR). We found that AICAR did not affect the amplitude (Figure 4C, Rod AICAR) or the response waveform (Figure 4D, Rod AICAR). Therefore, the 2-DG-induced slowdown of the rod response is independent of the AMPK activity.

Discussion

In this study, we characterized the fluorescent distributions of the hyBRET-AMPK and GO-ATeam2 retinas (Figure 1) and validated the function of the hyBRET-AMPK biosensor in live retinal explants (Figure 2A–C). Responses to three representative AMPK activators were visualized, and characteristic ATP responses were observed (Figure 2D–F). Single cell resolution analysis revealed that the 2-DG-induced response was markedly larger in rods than in cones (Figure 3). Consistent with this finding, 2-DG slowed down the dim flash response specifically in rods (Figure 4). In summary, these data support the notion that cones are less dependent on glycolysis than rods. Our data also suggest that, upon glycolysis inhibition, rods quickly modify their metabolic program to recover the ATP level and physiological performance.

Our methods provided a unique opportunity to depict the cellular heterogeneity in the retinal metabolic ecosystem. PNA-Alexa staining enabled a rod–cone comparison in the rod-dominant mouse retina (Figure 3), which would not have been achievable using the conventional oxygen microelectrode method. The comparison of Müller cells and neurons in the IPL would also be possible by the strong fluorescence from Müller cells (Figures 1 and S4). The applications can be expanded by combining this approach with the cell type-specific expression of the FRET biosensor (33) and simultaneous multicolor measurements with a red-shifted sensor variant (34). However, a major technical limitation of the two-photon excitation microscopy is the concomitant activation of the phototransduction cascade (35). The estimated rhodopsin activation is 1×10^3 R* rod^{-1} scan^{-1} under our typical imaging condition (26). Measurements should be interpreted with this constraint if the readout is strongly affected by the phototransduction (e.g., Ca^{2+}, voltage).

The AMPK imaging visualized characteristic temporal patterns of the AMPK activation by three common AMPK activators (Figure 2B). The glycolysis inhibitor, 2-DG, activated AMPK in the PRS more quickly and significantly than in the other layers (Figure 2B, left). This is consistent with the previous finding that the rate of glycolysis was higher than the rate of OXPHOS in photoreceptor cells (6). In contrast, AICAR activated AMPK in the PRS more slowly than in the other layers (Figure 2B, center). After the uptake, AICAR has to be converted to 5-amino-4-imidazolecarboxamide ribotide to bind and activate AMPK (36). The incorporation

14

and/or conversion of AICAR might be slow in the PRS than in the IPL and GCL. Metformin activated AMPK more slowly than the other two activators (Figure 2B, right). This might be due to slow metformin accumulation into the mitochondria (37).

The ATP imaging also visualized characteristic patterns for each of the three drugs. 2-DG reduced the ATP level in the retina (Figure 2D–F, left), as reported previously (38, 39). AICAR showed only limited effects on the ATP level (Figure 2D–F, center), which is consistent with the previous report that AICAR activates AMPK directly without inhibiting either glycolysis or OXPHOS (36). Metformin increased the ATP level (Figure 2D–F, right). In agreement with this finding, retinal ATP is known to increase 2 h after a subcutaneous metformin injection (40), which might be caused by an upregulation of glycolysis (41, 42). Notably, the ATP level began to decrease only in the IPL at 100 min, suggesting the cell type specificity in the response to metformin.

The 2-DG-induced AMPK activation and ATP reduction were significantly less in cones than in rods (Figure 3). Accordingly, 2-DG transiently prolonged the dim flash response in rods but not in cones (Figure 4). Since 2-DG is a glucose analog that inhibits glycolysis (36), a simple explanation of these results is that the cones produce ATP primarily via mitochondrial OXPHOS using the pyruvate and amino acids in the perfusion solution, DMEM/F12. However, this interpretation argues against the previous estimation that the cone-dominant ground squirrel retina uses about 95% of glucose through glycolysis (19). This rate of glycolysis is comparable to that in the rod-dominant retina (43). Therefore, we propose that cones become less dependent on glycolysis when surrounded by highly glycolytic rods. In line with this model, the oxygen consumption rate of photoreceptor cells is higher in the rod-cone mixed perifoveal region than in the 100% cone foveal region of the macaque retina (44), suggesting that perifoveal cones rely more on OXPHOS. Moreover, cone-specific deletion of basigin to inhibit lactate export and thus glycolysis does not display a degenerative phenotype, whereas the rod-specific counterpart does (45). Further single-cell resolution studies will be needed to clarify the cone metabolism in the rod-dominant environment.

Rods showed marked recoveries in both AMPK activity and ATP level, starting as early as 30 min from the onset of 2-DG perfusion (Figure 3). Several lines of evidence suggest that AMPK activation upregulates the use

of non-glucose energy substrates through OXPHOS. In mouse primary neuron culture, AMPK activation upregulates mitochondrial respiration as well as glycolysis (46). On the other hand, AMPK knockdown in a photoreceptor-derived cell line, 661W, reduces the cytochrome c oxidase activity (47). In mouse cones, a 24 h fast induces the AMPK activation and macroautophagy (48). Based on these evidences, we speculate that the strong AMPK activation in rods upregulates autophagy and OXPHOS to support the ATP recovery. In support of this model, a recent imaging study revealed the dynamic interplay between autophagy and the ATP/ADP levels in migrating neurons (49). The detailed mechanism underlying the rod ATP recovery will be addressed in our future study using specific inhibitors of autophagy and OXPHOS enzymes.

What is the link between ATP reduction (Figure 3D–F) and slow rod photoresponse (Figure 4B–D, WT Rod 2-DG)? The involvement of AMPK is ruled out because the photoresponse was not slowed down by AICAR (Figure 4B–D, Rod AICAR). Among the various phototransduction proteins, there is one, G-protein receptor kinase 1 (GRK1), that uses ATP to phosphorylate photoactivated rhodopsin. However, the Michaelis constant (K_m) of GRK1 for ATP is 10.6 μM (50). Thus, GRK1 activity is not likely to be affected, because the ATP reduction observed in this study was within the millimolar-order dynamic range of the GO-ATeam2 biosensor (31). Another possible link is guanylate cyclase (GC), which synthesizes cGMP to terminate the photoresponse. Although the substrate of GC is GTP, the GTP level can be reduced when the ATP level drops. This is because nucleoside diphosphate kinase, which maintains the balance of NTPs by transphosphorylation from NTP to NDP, is widely expressed in the retina (51). Indeed, parallel behavior of ATP and GTP levels was reported in frog rods (52). The K_m of GC for GTP ranges from 0.63 to 3.18 mM depending on the presence or absence of GC activating proteins (53). This range is comparable to the estimated GTP concentration in photoreceptor cells, 0.5 to 1.2 mM, based on the molar ratio of GTP and rhodopsin (54, 55) and the rhodopsin concentration (8) in the rod outer segment. Therefore, we speculate that the slowdown in the rod photoresponse is mediated by the reduced GTP level, which slows down the cGMP synthesis by GC.

As exemplified by the large mitochondrial mass (16), glycogen storage (56), and cone-specific visual cycle (57), cones have a number of metabolic mechanisms that rods do not have. However, access to these topics is

16

technically limited, particularly in the rod-dominant mouse retina. A single cell-resolution imaging approach, with a variety of FRET biosensors (58), will become a good option for better understanding of the complex metabolic ecosystem in the retina.

References

1. Okawa, H., Sampath, A. P., Laughlin, S. B., and Fain, G. L. (2008) ATP consumption by mammalian rod photoreceptors in darkness and in light. *Curr Biol* **18**, 1917-1921

2. Ingram, N. T., Fain, G. L., and Sampath, A. P. (2020) Elevated energy requirement of cone photoreceptors. *Proc Natl Acad Sci U S A* **117**, 19599-19603

3. Hurley, J. B., Lindsay, K. J., and Du, J. (2015) Glucose, lactate, and shuttling of metabolites in vertebrate retinas. *J Neurosci Res* **93**, 1079-1092

4. Pan, W. W., Wubben, T. J., and Besirli, C. G. (2021) Photoreceptor metabolic reprogramming: current understanding and therapeutic implications. *Commun Biol* **4**, 245

5. Viegas, F. O., and Neuhauss, S. C. F. (2021) A Metabolic Landscape for Maintaining Retina Integrity and Function. *Front Mol Neurosci* **14**, 656000

6. Narayan, D. S., Chidlow, G., Wood, J. P., and Casson, R. J. (2017) Glucose metabolism in mammalian photoreceptor inner and outer segments. *Clin Exp Ophthalmol* **45**, 730-741

7. Chinchore, Y., Begaj, T., Wu, D., Drokhlyansky, E., and Cepko, C. L. (2017) Glycolytic reliance promotes anabolism in photoreceptors. *Elife* **6**, e25946

8. Nickell, S., Park, P. S., Baumeister, W., and Palczewski, K. (2007) Three-dimensional architecture of murine rod outer segments determined by cryoelectron tomography. *J Cell Biol* **177**, 917-925

9. Mazzolini, M., Facchetti, G., Andolfi, L., Proietti Zaccaria, R., Tuccio, S., Treu, J., Altafini, C., Di Fabrizio, E. M., Lazzarino, M., Rapp, G., and Torre, V. (2015) The phototransduction machinery in the rod outer segment has a strong efficacy gradient. *Proc Natl Acad Sci U S A* **112**, E2715-2724

10. Kanow, M. A., Giarmarco, M. M., Jankowski, C. S., Tsantilas, K., Engel, A. L., Du, J., Linton, J. D., Farnsworth, C. C., Sloat, S. R., Rountree, A., Sweet, I. R., Lindsay, K. J., Parker, E. D., Brockerhoff, S. E., Sadilek, M., Chao, J. R., and Hurley, J. B. (2017) Biochemical adaptations of the retina and retinal pigment epithelium support a metabolic ecosystem in the vertebrate eye. *Elife* **6**, e28899

11. Bisbach, C. M., Hass, D. T., Robbings, B. M., Rountree, A. M., Sadilek, M., Sweet, I. R., and Hurley, J. B. (2020) Succinate Can Shuttle Reducing Power from the Hypoxic Retina to the O2-Rich Pigment Epithelium. *Cell Rep* **31**, 107606

12. Reyes-Reveles, J., Dhingra, A., Alexander, D., Bragin, A., Philp, N. J., and Boesze-Battaglia, K. (2017) Phagocytosis-dependent ketogenesis in retinal pigment epithelium. *J Biol Chem* **292**, 8038-8047

13. Yam, M., Engel, A. L., Wang, Y., Zhu, S., Hauer, A., Zhang, R., Lohner, D., Huang, J., Dinterman, M., Zhao, C., Chao, J. R., and Du, J. (2019) Proline mediates metabolic communication between retinal pigment epithelial cells and the retina. *J Biol Chem* **294**, 10278-10289

14. Masuda, T., Wada, Y., and Kawamura, S. (2016) ES1 is a mitochondrial enlarging factor contributing to form mega-mitochondria in zebrafish cones. *Sci Rep* **6**, 22360

15. Perkins, G. A., Ellisman, M. H., and Fox, D. A. (2003) Three-dimensional analysis of mouse rod and cone mitochondrial cristae architecture: bioenergetic and functional implications. *Mol Vis* **9**, 60-73

16. Hoang, Q. V., Linsenmeier, R. A., Chung, C. K., and Curcio, C. A. (2002) Photoreceptor inner segments

in monkey and human retina: mitochondrial density, optics, and regional variation. *Vis Neurosci* **19**, 395-407

17. Li, B., Zhang, T., Liu, W., Wang, Y., Xu, R., Zeng, S., Zhang, R., Zhu, S., Gillies, M. C., Zhu, L., and Du, J. (2020) Metabolic Features of Mouse and Human Retinas: Rods versus Cones, Macula versus Periphery, Retina versus RPE. *iScience* **23**, 101672

18. Petit, L., Ma, S., Cipi, J., Cheng, S. Y., Zieger, M., Hay, N., and Punzo, C. (2018) Aerobic Glycolysis Is Essential for Normal Rod Function and Controls Secondary Cone Death in Retinitis Pigmentosa. *Cell Rep* **23**, 2629-2642

19. Winkler, B. S., Starnes, C. A., Twardy, B. S., Brault, D., and Taylor, R. C. (2008) Nuclear magnetic resonance and biochemical measurements of glucose utilization in the cone-dominant ground squirrel retina. *Invest Ophthalmol Vis Sci* **49**, 4613-4619

20. Xu, L., and Ash, J. D. (2016) The Role of AMPK Pathway in Neuroprotection. *Adv Exp Med Biol* **854**, 425-430

21. Konagaya, Y., Terai, K., Hirao, Y., Takakura, K., Imajo, M., Kamioka, Y., Sasaoka, N., Kakizuka, A., Sumiyama, K., Asano, T., and Matsuda, M. (2017) A Highly Sensitive FRET Biosensor for AMPK Exhibits Heterogeneous AMPK Responses among Cells and Organs. *Cell Rep* **21**, 2628-2638

22. Yamamoto, M., Kim, M., Imai, H., Itakura, Y., and Ohtsuki, G. (2019) Microglia-Triggered Plasticity of Intrinsic Excitability Modulates Psychomotor Behaviors in Acute Cerebellar Inflammation. *Cell Rep* **28**, 2923-2938

23. Komatsu, N., Terai, K., Imanishi, A., Kamioka, Y., Sumiyama, K., Jin, T., Okada, Y., Nagai, T., and Matsuda, M. (2018) A platform of BRET-FRET hybrid biosensors for optogenetics, chemical screening, and in vivo imaging. *Sci Rep* **8**, 8984

24. Sumiyama, K., Kawakami, K., and Yagita, K. (2010) A simple and highly efficient transgenesis method in mice with the Tol2 transposon system and cytoplasmic microinjection. *Genomics* **95**, 306-311

25. Calvert, P. D., Krasnoperova, N. V., Lyubarsky, A. L., Isayama, T., Nicolo, M., Kosaras, B., Wong, G., Gannon, K. S., Margolskee, R. F., Sidman, R. L., Pugh, E. N., Jr., Makino, C. L., and Lem, J. (2000) Phototransduction in transgenic mice after targeted deletion of the rod transducin alpha -subunit. *Proc Natl Acad Sci U S A* **97**, 13913-13918

26. Sato, S., Yamashita, T., and Matsuda, M. (2020) Rhodopsin-mediated light-off-induced protein kinase A activation in mouse rod photoreceptor cells. *Proc Natl Acad Sci U S A* **117**, 26996-27003

27. Parslow, A., Cardona, A., and Bryson-Richardson, R. J. (2014) Sample drift correction following 4D confocal time-lapse imaging. *J Vis Exp*, 51086

28. Vinberg, F., Kolesnikov, A. V., and Kefalov, V. J. (2014) Ex vivo ERG analysis of photoreceptors using an in vivo ERG system. *Vision Res* **101**, 108-117

29. Vinberg, F., and Kefalov, V. (2015) Simultaneous ex vivo functional testing of two retinas by in vivo electroretinogram system. *J Vis Exp*, e52855

30. Becker, S., Carroll, L. S., and Vinberg, F. (2020) Rod phototransduction and light signal transmission

during type 2 diabetes. *BMJ Open Diabetes Res Care* **8**, e001571

31. Nakano, M., Imamura, H., Nagai, T., and Noji, H. (2011) Ca(2)(+) regulation of mitochondrial ATP synthesis visualized at the single cell level. *ACS Chem Biol* **6**, 709-715

32. Johnson, L. V., Hageman, G. S., and Blanks, J. C. (1986) Interphotoreceptor matrix domains ensheath vertebrate cone photoreceptor cells. *Invest Ophthalmol Vis Sci* **27**, 129-135

33. Konishi, Y., Terai, K., Furuta, Y., Kiyonari, H., Abe, T., Ueda, Y., Kinashi, T., Hamazaki, Y., Takaori-Kondo, A., and Matsuda, M. (2018) Live-Cell FRET Imaging Reveals a Role of Extracellular Signal-Regulated Kinase Activity Dynamics in Thymocyte Motility. *iScience* **10**, 98-113

34. Watabe, T., Terai, K., Sumiyama, K., and Matsuda, M. (2020) Booster, a Red-Shifted Genetically Encoded Forster Resonance Energy Transfer (FRET) Biosensor Compatible with Cyan Fluorescent Protein/Yellow Fluorescent Protein-Based FRET Biosensors and Blue Light-Responsive Optogenetic Tools. *ACS Sens* **5**, 719-730

35. Euler, T., Franke, K., and Baden, T. (2019) Studying a Light Sensor with Light: Multiphoton Imaging in the Retina. In *Multiphoton Microscopy* (Hartveit, E., ed) pp. 225-250, Springer New York, New York, NY

36. Bost, F., Decoux-Poullot, A. G., Tanti, J. F., and Clavel, S. (2016) Energy disruptors: rising stars in anticancer therapy? *Oncogenesis* **5**, e188

37. Owen, M. R., Doran, E., and Halestrap, A. P. (2000) Evidence that metformin exerts its anti-diabetic effects through inhibition of complex 1 of the mitochondrial respiratory chain. *Biochem J* **348 Pt 3**, 607-614

38. Chertov, A. O., Holzhausen, L., Kuok, I. T., Couron, D., Parker, E., Linton, J. D., Sadilek, M., Sweet, I. R., and Hurley, J. B. (2011) Roles of Glucose in Photoreceptor Survival. *Journal of Biological Chemistry* **286**, 34700-34711

39. Winkler, B. S. (1981) Glycolytic and oxidative metabolism in relation to retinal function. *J Gen Physiol* **77**, 667-692

40. Xu, L., Kong, L., Wang, J., and Ash, J. D. (2018) Stimulation of AMPK prevents degeneration of photoreceptors and the retinal pigment epithelium. *Proc Natl Acad Sci U S A* **115**, 10475-10480

41. Andrzejewski, S., Gravel, S. P., Pollak, M., and St-Pierre, J. (2014) Metformin directly acts on mitochondria to alter cellular bioenergetics. *Cancer Metab* **2**, 12

42. Li, W. J., Chaudhari, K., Shetty, R., Winters, A., Gao, X. F., Hu, Z. N., Ge, W. P., Sumien, N., Forster, M., Liu, R., and Yang, S. H. (2019) Metformin Alters Locomotor and Cognitive Function and Brain Metabolism in Normoglycemic Mice. *Aging Dis* **10**, 949-963

43. Wang, L., Kondo, M., and Bill, A. (1997) Glucose metabolism in cat outer retina. Effects of light and hyperoxia. *Invest Ophthalmol Vis Sci* **38**, 48-55

44. Birol, G., Wang, S., Budzynski, E., Wangsa-Wirawan, N. D., and Linsenmeier, R. A. (2007) Oxygen distribution and consumption in the macaque retina. *Am J Physiol Heart Circ Physiol* **293**, H1696-1704

45. Han, J. Y. S., Kinoshita, J., Bisetto, S., Bell, B. A., Nowak, R. A., Peachey, N. S., and Philp, N. J. (2020)

Role of monocarboxylate transporters in regulating metabolic homeostasis in the outer retina: Insight gained from cell-specific Bsg deletion. *FASEB J* **34**, 5401-5419

46. Marinangeli, C., Didier, S., Ahmed, T., Caillerez, R., Domise, M., Laloux, C., Begard, S., Carrier, S., Colin, M., Marchetti, P., Ghesquiere, B., Balschun, D., Buee, L., Kluza, J., and Vingtdeux, V. (2018) AMP-Activated Protein Kinase Is Essential for the Maintenance of Energy Levels during Synaptic Activation. *iScience* **9**, 1-13

47. Kawashima, H., Ozawa, Y., Toda, E., Homma, K., Osada, H., Narimatsu, T., Nagai, N., and Tsubota, K. (2020) Neuroprotective and vision-protective effect of preserving ATP levels by AMPK activator. *FASEB J* **34**, 5016-5026

48. Zhou, Z., Vinberg, F., Schottler, F., Doggett, T. A., Kefalov, V. J., and Ferguson, T. A. (2015) Autophagy supports color vision. *Autophagy* **11**, 1821-1832

49. Bressan, C., Pecora, A., Gagnon, D., Snapyan, M., Labrecque, S., De Koninck, P., Parent, M., and Saghatelyan, A. (2020) The dynamic interplay between ATP/ADP levels and autophagy sustain neuronal migration in vivo. *Elife* **9**

50. Horner, T. J., Osawa, S., Schaller, M. D., and Weiss, E. R. (2005) Phosphorylation of GRK1 and GRK7 by cAMP-dependent protein kinase attenuates their enzymatic activities. *J Biol Chem* **280**, 28241-28250

51. Rueda, E. M., Johnson, J. E., Jr., Giddabasappa, A., Swaroop, A., Brooks, M. J., Sigel, I., Chaney, S. Y., and Fox, D. A. (2016) The cellular and compartmental profile of mouse retinal glycolysis, tricarboxylic acid cycle, oxidative phosphorylation, and ~P transferring kinases. *Mol Vis* **22**, 847-885

52. Biernbaum, M. S., and Bownds, M. D. (1985) Frog rod outer segments with attached inner segment ellipsoids as an in vitro model for photoreceptors on the retina. *J Gen Physiol* **85**, 83-105

53. Peshenko, I. V., Olshevskaya, E. V., Savchenko, A. B., Karan, S., Palczewski, K., Baehr, W., and Dizhoor, A. M. (2011) Enzymatic properties and regulation of the native isozymes of retinal membrane guanylyl cyclase (RetGC) from mouse photoreceptors. *Biochemistry* **50**, 5590-5600

54. Biernbaum, M. S., and Bownds, M. D. (1979) Influence of light and calcium on guanosine 5'-triphosphate in isolated frog rod outer segments. *J Gen Physiol* **74**, 649-669

55. Salceda, R., van Roosmalen, G. R., Jansen, P. A., Bonting, S. L., and Daemen, F. J. (1982) Nucleotide content of isolated bovine rod outer segments. *Vision Res* **22**, 1469-1474

56. Okubo, A., Sameshima, M., Unoki, K., Uehara, F., and Ohba, N. (1998) Ultracytochemical demonstration of glycogen in cone, but not in rod, photoreceptor cells in the rat retina. *Ann Anat* **180**, 307-314

57. Morshedian, A., Kaylor, J. J., Ng, S. Y., Tsan, A., Frederiksen, R., Xu, T., Yuan, L., Sampath, A. P., Radu, R. A., Fain, G. L., and Travis, G. H. (2019) Light-Driven Regeneration of Cone Visual Pigments through a Mechanism Involving RGR Opsin in Muller Glial Cells. *Neuron* **102**, 1172-1183 e1175

58. Terai, K., Imanishi, A., Li, C., and Matsuda, M. (2019) Two Decades of Genetically Encoded Biosensors Based on Forster Resonance Energy Transfer. *Cell Struct Funct* **44**, 153-169

Tables

Table 1 Laser wavelengths and optical filters.

Data	Figure 1A, B	Figures 2A and 3A	Figures 1C, D, and 3D	Figure 2C
FRET biosensor	hyBRET-AMPK	hyBRET-AMPK	GO-ATeam2	GO-ATeam2
System	FV1200MPE-BX61	FV1000MPE-BX61	FV1200MPE-BX61	FV1000MPE-BX61
Laser 1 (nm)	840	840	930	930
Laser 2 (nm)	(N/A)	(N/A)	1040	(N/A)
Dichroic mirror 1	DM450[†]	DM450[†]	DM450[†]	DM485[†]
Dichroic mirror 2	DM505[†]	DM505[†]	DM550[†]	DM570[†]
Dichroic mirror 3	DM570[†]	DM570[†]	DM610[†]	DM570[†]
Filter 1	BA460-500[†] for CFP Ch[§]	BA460-500[†] for CFP Ch	BA495-540HQ[†] for GFP Ch[§]	BA495-540HQ[†] for GFP Ch
Filter 2	BA520-560[†] for FRET Ch[§]	BA520-560[†] for FRET Ch	FF01-579/34[‡] for FRET Ch[§]	BA575-630[†] for FRET Ch
Filter 3	(N/A)	(N/A) for Alexa568 Ch	FF01-647/57[‡] for Alexa594 Ch	(N/A)

[†]Olympus,[‡]Semrock,[§]GaAsP detectors

Table 2 Parameters of the AMPK response.

		2-DG	AICAR	Metformin
Amplitude (ΔFRET/CFP)	GCL	0.062 ± 0.012	0.21 ± 0.02	0.22 ± 0.04
	IPL	0.039 ± 0.012	0.13 ± 0.01	0.13 ± 0.03
	PRS	0.21 ± 0.02[†]	0.18 ± 0.01	0.18 ± 0.03
Time constant (min)	GCL	13 ± 2	12 ± 2	85 ± 30
	IPL	8.0 ± 6.9	14 ± 1	29 ± 7
	PRS	0.92 ± 0.41[†]	31 ± 3	61 ± 10

Mean $\pm$ SD (n = 5 or 6 viewfields from 2 retinas).
[†]Data points up to 50 min were used for fittings.

Figure legends

Figure 1 Ubiquitous expression of hyBRET-AMPK and GO-ATeam2 biosensors in the retina. (A) Two-photon fluorescent images from six layers of the hyBRET-AMPK retina. (B) Longitudinal view reconstructed from the Z-stack images. Z interval = 1 μm. (C and D) Corresponding images of the GO-ATeam2 retinas. GCL: ganglion cell layer; IPL: inner plexiform layer; INL: inner nuclear layer; OPL: outer plexiform layer; ONL: outer nuclear layer; PRS: photoreceptor segments.

Figure 2 Spatiotemporal regulation of the AMPK activity and ATP level by three AMPK activators. (A) Time-lapse montage images of the longitudinal view from hyBRET-AMPK retinas. Z interval: 4 μm; time interval: 10 min. The AMPK activity is visualized as the ratio of fluorescent signals from the FRET acceptor YFP (FRET) to fluorescent signals from the FRET donor CFP (CFP), and shown in rainbow pseudo-color. The indicated activator was perfused from time 0 for 80 min (2-DG), for 90 min (AICAR), or for 210 min (metformin). (B) Time courses of the FRET ratios at the layers indicated in (A). Mean of 5–6 view fields from 2 retinas. (C) AMPK activity before and after the drug perfusion. Basal: an average of -30 to 0 min; 2-DG: an average of 60 to 80 min; AICAR: an average of 70 to 90 min; metformin: an average of 190 to 210 min. Each dot represents the activity measured from one view field. Value on the bars are the P-values for the two-tailed paired t-test. n = 5–6 view fields from 2 retinas. (D–F) Corresponding data from GO-ATeam2 retinas. Z interval: 6 μm (2-DG and AICAR) or 4 μm (metformin); time interval: 10 min. n = 5–8 view fields from 2 retinas. The ratio of signals from the FRET acceptor mKOκ (FRET) to signals from the FRET donor GFP (GFP) was used for visualization.

Figure 3 Different AMPK and ATP responses to 2-DG between rods and cones. (A) High magnification XY view at the PRS in the hyBRET-AMPK retina. 2-DG was perfused from time 0 min to 80 min. PNA-Alexa568 signals on cone sheaths were used for the rod-cone segmentation. (B) Time courses of the FRET ratio in rods and cones. Mean ± SD, n = 10 view fields from 3 retinas. (C) Amplitude of the response and recovery. The response is defined as the difference between the FRET/CFP at 20 min and that at 0 min ($R_{20 min}$ - $R_{0 min}$).

Recovery is defined as $R_{20\ min}$ - $R_{80\ min}$. Each dot represents the value obtained from one view field. Values on the bars are P-values for the two-tailed paired t-test. (D–F) Corresponding data from GO-ATeam2 retinas. n = 9 view fields from 3 retinas. Response and recovery are shown as absolute values.

Figure 4 Rod-specific slowdown in dim flash responses of the *ex vivo* ERG recordings. (A) Responses to 2-DG at the PRS in the hyBRET-AMPK and GO-ATeam2 retinas. Data from dark-adapted specimens are shown as red curves. Mean ± SD, n = 2 retinas. Corresponding data from light-adapted specimens in Figure 2 are overlaid as black dashed curves with SD for comparison. (B) Superimposed dim flash responses of photoreceptor cells obtained at the indicated time points. Traces are average of recordings from 5 retinas. The arrow shows the timing of the 2 ms 500 nm flash stimulation. Flashes of 10 and 1000 photons μm^{-2} were used in order to elicit WT rod responses and *Gnat1*$^{-/-}$ cone responses, respectively. The drug indicated in each panel was delivered from 0 min to 60 min. (C and D) Time courses of the photoresponse amplitude (C) and integration time (D). Dim flash responses were obtained every 20 s, and 6 responses were averaged for these analyses. Mean ± SD, n = 5 retinas.
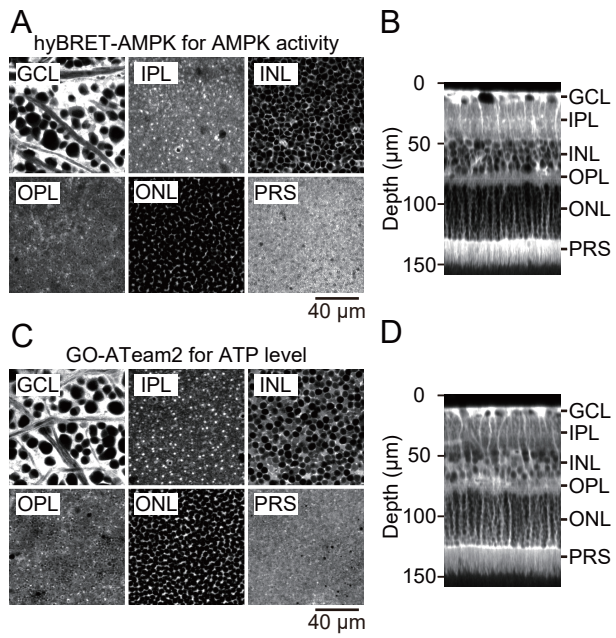
A hyBRET-AMPK for AMPK activity

GCL   IPL   INL

OPL   ONL   PRS

40 µm

B

Depth (µm)

0 — GCL
    — IPL
50 — INL
    — OPL
100 — ONL
    — PRS
150 —

C GO-ATeam2 for ATP level

GCL   IPL   INL

OPL   ONL   PRS

40 µm

D

Depth (µm)

0 — GCL
    — IPL
50 — INL
    — OPL
100 — ONL
    — PRS
150 —

Figure 1 He et al.

Figure 2 He et al.

Figure 3 He et al.

A

10 mM
2-DG

AMPK activity
(FRET/CFP)

- - - Light
— Dark

ATP level
(FRET/GFP)

Time (min)

B

10
photons μm⁻²

WT
Rod
control

-5 min   35 min
5 min   45 min
15 min   55 min
25 min

10

WT
Rod
2-DG

1000

Gnat1⁻/⁻
Cone
2-DG

10

WT
Rod
AICAR

100 μV

0.5 s

C

Photoresponse

Rod control

10 mM 2-DG

- - - Rod control
— Rod 2-DG

Photoresponse (μV)

10 mM 2-DG

Cone 2-DG

1 mM AICAR

- - - Rod control
— Rod AICAR

Time (min)

D

Integration time

1

Rod control

10 mM 2-DG

- - - Rod control
— Rod 2-DG

Integration time (ms)

10 mM 2-DG

Cone 2-DG

1 mM AICAR

- - - Rod control
— Rod AICAR
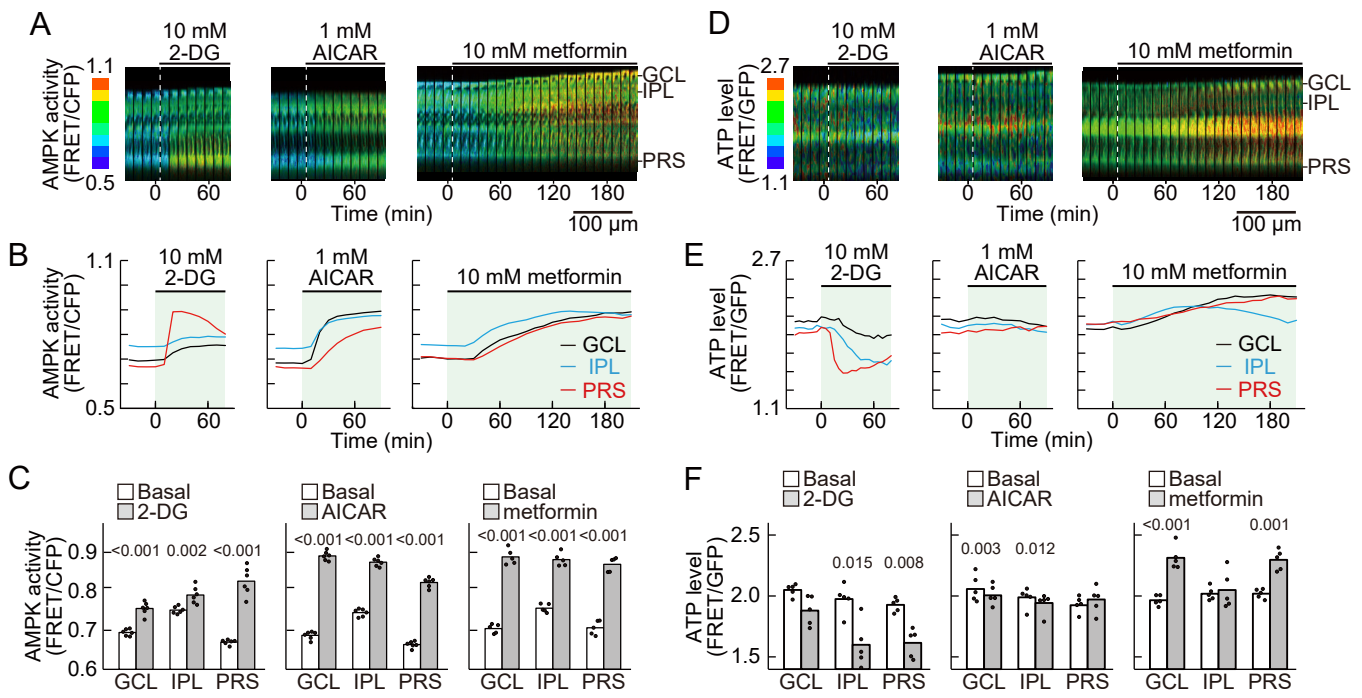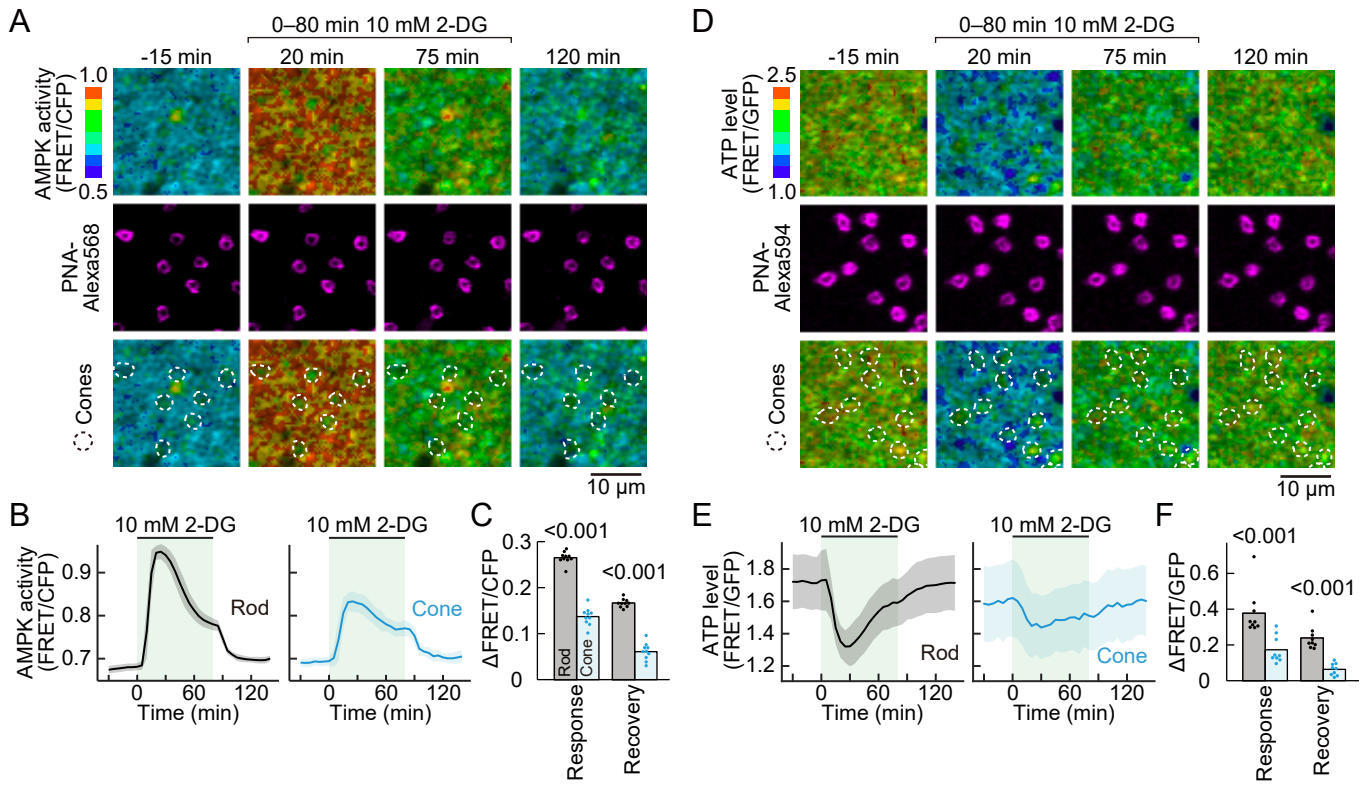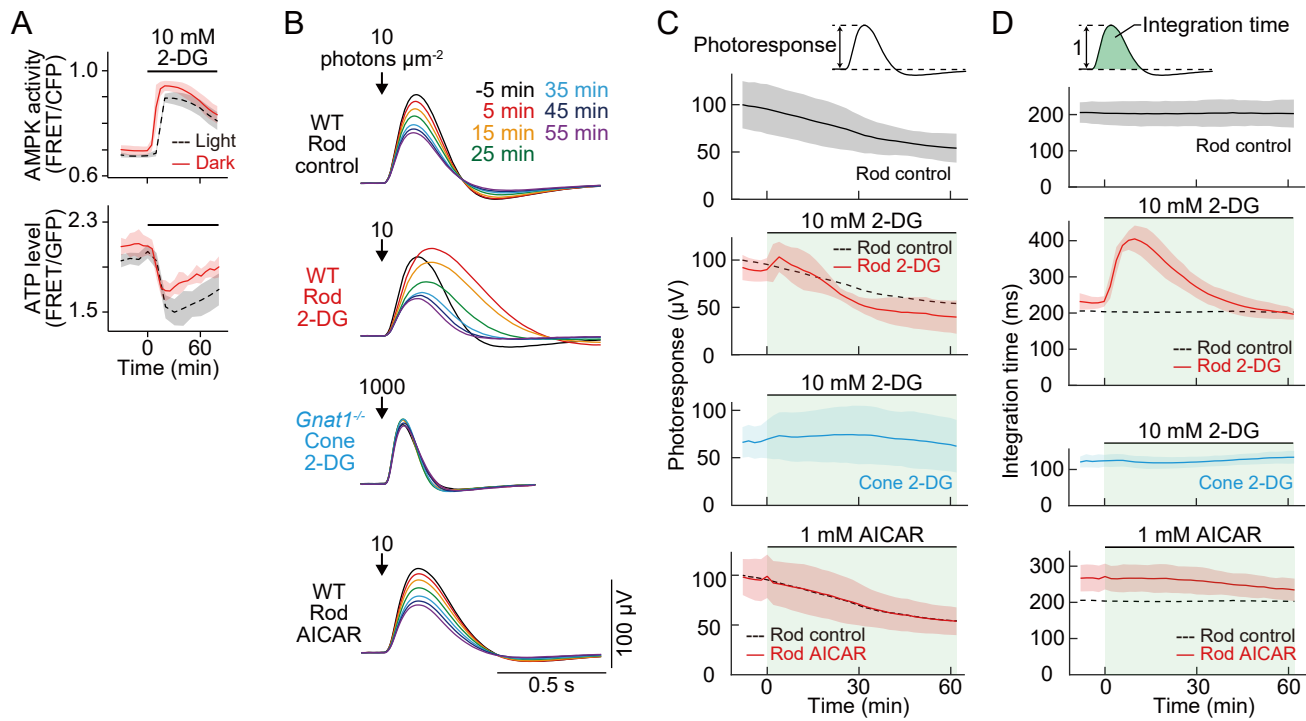
Time (min)

Figure 4 He et al.

1   **Supplemental Information**

2   This file includes:

3   Supplemental Methods

4   Figures S1 to S5

5   Tables S1 to S2

6   Supplemental References

7

8   **Supplemental Methods**

9   **Reagents**

10   Catalog numbers and suppliers of other reagents are listed in Table S1.

11   **Table S1** List of reagents

Reagent	Cat#	Supplier
Isoflurane	095-06573	FUJIFILM Wako Pure Chemical (Osaka, Japan)
Dulbecco's modified Eagle's medium/nutrient mixture F-12 Ham (DMEM/F12)	D2906	Sigma-Aldrich (St. Louis, MO, USA)
Penicillin-streptomycin mixed solution	26253-84	Nacalai Tesque (Kyoto, Japan)
Sodium bicarbonate (NaHCO$_3$)	31212-25	Nacalai Tesque
2-Deoxy-D-glucose (2-DG)	D8375-1G	Sigma-Aldrich
	D0051	Tokyo Chemical Industry (Tokyo, Japan)
5-Aminoimidazole-4-carboxamide-1-β-D-ribofuranoside (AICAR)	011-22533	FUJIFILM Wako Pure Chemical
Metformin hydrochloride	138-15481	Wako Pure Chemical Industries (Osaka, Japan)
PNA-Alexa568	L32458	Thermo Fisher Scientific (Waltham, MA, USA)
PNA-Alexa594	L32459	Thermo Fisher Scientific
Phosphate-buffered saline (PBS)	T900	Takara Bio
4% Paraformaldehyde phosphate buffer solution	163-20145	FUJIFILM Wako Pure Chemical
O.C.T compound (OCT)	4583	Sakura Finetek (Tokyo, Japan)
Normal goat serum	555-76251	FUJIFILM Wako Chemical
Triton X-100	35501-15	Nacalai Tesque
RLBP1 polyclonal antibody (RRID: AB_2178530)	15356-1-AP	Proteintech (Rosemont, IL, USA)
Goat anti-rabbit IgG (H+L) highly cross-adsorbed secondary antibody Alexa Fluor 647 (Alexa647-anti-rabbit IgG; RRID: AB_2535813)	A21245	Thermo Fisher Scientific
Vectershield	H-1000	Vector Laboratories (Burlingame, CA, USA)
Barium chloride	025-00172	FUJIFILM Wako Pure Chemical
DL-2-amino-4-phosphonobutyric acid (DL-AP4)	ab120001	Abcam (Cambridge, MA, USA)

12

Animals

Mice (*Mus musculus*) were housed in a specific-pathogen-free facility with a 14/10 h light-dark cycle and fed a standard laboratory chow diet and water *ad libitum*. Male and female mice were used at the age of 1–6 months. Wild type C57BL/6J (B6J) mice were obtained from Charles River Laboratories Japan and Japan SLC (Hamamatsu, Shizuoka, Japan).

The albino hyBRET-AMPK mouse (nbio327; NIBIOHN) was bred with a normal pigmented B6J mouse to remove the *rd8* mutation (a single base deletion at nt3481 on *Crb1*) (Mattapallil et al., 2012) and albino mutation (a G291T point mutation on *Tyr*) (Le Fur et al., 1996). Removal of both mutations was verified by Sanger sequencing of genomic DNA using the primer sets shown in Table S2.

GO-Ateam2 mice (1) were maintained as homozygous mice by inbreeding. The first breeding pair of homozygous mice was selected by genotyping PCR using the primers listed in Table S2.

Table S2 A list of PCR primers

PCR	Direction	Sequence
rd8 sequencing	Forward	5′-ACCTGATGGGTTCCCAATTG-3′
	Reverse	5′-AACCAGCCTTGTTTAGCACC-3′
Albino sequencing	Forward	5′-GGGGTTGCTGGAAAAGAAGTCTGTG-3′
	Reverse	5′-TGTGGGGATGACATAGACTGAGCTG-3′
GO-ATeam2 genotyping wild type allele	Forward	5′-ATTCTGCTTACATAGTCTAACTCGC-3′
	Reverse	5′-TGGGCAGGCTTAAAGGCTAA-3′
GO-ATeam2 genotyping transgene positive allele	Forward	5′-TTCCCTCGTGATCTGCAACT-3′
	Reverse	5′-AACTCGGGTGAGCATGTCTTT-3′

Perfusion system for live imaging

The following modifications were added to the method in our recent paper (2). The perfusion solution was split into two bottles, one of which was supplemented with the drug indicated in each figure. Aqueous stock solutions of drugs were prepared at 2.5 M for 2-DG and metformin and at 50 mM for AICAR. They were stored at -20 °C until added. A square polystyrene dish (1-1824698-01; As One, Osaka, Japan) was adhered on a circular metal plate (SZ304; Hikari, Osaka, Japan) and used as the perfusion chamber. In some experiments, a plate heater (TPX-S; Tokai Hit, Fujinomiya, Shizuoka, Japan) and a lens

3

37 warmer (TP-LH; Tokai Hit) were used to improve the temperature stability.

38

Immunohistochemistry

40 The isolated hyBRET-AMPK retina was fixed in 1 mL of 4% (w/v) paraformaldehyde

41 phosphate-buffered solution at room temperature for 15 min, washed in 1 mL PBS for 30

42 min, and dehydrated in 1 mL of 10%, 20% and 30% (w/v) sucrose in PBS for 30 min at

43 room temperature, 60 min at room temperature, and overnight at 4 °C, respectively. The

44 retina was incubated in 2 mL 50% (v/v) OCT in PBS at room temperature on a rotation

45 mixer, embedded in a plastic mold filled with OCT, and frozen in an isopentane bath

46 surrounded by liquid nitrogen. Sections 16 μm in thickness were cut from the block using a

47 Cryostar NX70 (Thermo Scientific) at -20 °C, adhered on an MAS adhesive glass slide

48 (MAS-01; Matsunami Glass, Kishiwada, Osaka, Japan), and dried with a blower for 60 min

49 at room temperature for better adherence. The sections were soaked in 80 mL PBS 2 times,

50 outlined with Super PAP Pen Mini (S-PAP-M; Daido Sangyo, Toda, Saitama, Japan), and

51 mounted with 25 µL blocking solution (5% (v/v) normal goat serum, 0.3% (v/v) Triton X-

52 100 in PBS) for 60 min followed by 25 µL of primary antibody solution (1% (v/v) RLBP1

53 polyclonal antibody, 0.3% (v/v) Triton X-100 in PBS) for 4 h at room temperature. The

54 slides were kept in a humidified box when the incubation time was 60 min or longer. The

55 sections were then soaked in 80 mL wash solution (0.025% (v/v) Triton X-100 in PBS)

56 three times for 5 min each, mounted with 25 µL of secondary antibody solution (0.33%

57 (v/v) Alexa647-anti-rabbit IgG in PBS) for 60 min, washed three times again, and mounted

58 with a cover glass (C022221; Matsunami Glass) with 10 µL of the Vectashield.

59   The labeled retinal sections were imaged with an inverted confocal microscope system

60 (iFV1000; Olympus) using an UPLSAPO30XS objective lens (Olympus) and silicone

61 immersion oil (SIL300CS-30CC; Olympus). The hyBRET-AMPK biosensor was imaged

62 with a 405 nm excitation laser, and Alexa647 was sequentially imaged with a 635 nm

63 excitation laser. Images were processed on Fiji.

64

Acrylic retina holder for *ex vivo* ERG

66 The side length of our holder (Figure S3A) is about one half the length of Vinberg's holder

67 (3), because our version was designed to hold only one retina at a time. The filter paper

68 (HABG01300; Merck Millipore, Darmstadt, Hessen, Germany) at the top of the holder

69 dome was attached with double-sided sticky tape (NWBB-15; Nichiban, Tokyo, Japan)

4

70   instead of epoxy glue. To prepare a small circular piece of filter paper attached to a
71   doughnut-shape sticky tape, several holes ~1 mm in diameter were made on the tape with a
72   cautery pen, and a piece of the filter paper was attached to the tape. The paper was then
73   punched out in a 3 mm circular shape using a leather punch, with the hole on the tape at the
74   center.
75   The resulting circular filter paper was attached to the dome on the bottom part of the
76   retina holder (Figure S3A). A spent piece of filter paper were replaced as soon as damage
77   was apparent, typically once in ten experimental sessions.
78
79   **Perfusion system for *ex vivo* ERG**
80   Stock aqueous solutions of barium chloride and DL-AP4 were prepared at 100 mM and 10
81   mM, respectively, and stored at 4 °C until added. These inhibitors block the glial
82   component and b-wave component of the retinal photoresponse to isolate the photoreceptor
83   ERG component (3). DMEM/F12 powder was dissolved in water just before the
84   experiment, supplemented with the penicillin streptomycin mixture, barium chloride and
85   DL-AP4, and filtered through the bottle top filter. The solution was warmed up to 45 °C in
86   a water bath and calibrated at pH 7.4 by bubbling with the O_2/CO_2 gas mixture prior to the
87   recordings. The solution was then divided into two bottles and wrapped with USB electric
88   blankets to keep it warm during the recordings. The water bath was not used hereafter
89   because it may generate noise that could perturb the recordings. The drug indicated in each
90   figure was added into one of the bottles, and two bottles were connected to the perfusion
91   line through a three-way stopcock to switch solutions at scheduled time points.
92   The bottles were placed on a stage 50 cm higher than the retina holder, and the
93   perfusion was driven by gravity. The flow rate was adjusted at 1 to 1.5 mL/min manually
94   with a roller clamp (KT-4.5; AS ONE). The rate was monitored based on the weight of the
95   perfusion drain, which was recorded with an electronic scale. The perfusion was warmed
96   up in an inline heater inserted just before the retina holder, to keep the retina at 37 °C. The
97   temperature at the retina holder was calibrated by inserting a thin K-type thermocouple
98   wire into the perfusion line.
99
100 **Sample preparation and recordings of *ex vivo* ERG**
101 Two retinas were used in the rod recordings from B6J wild type retinas. One retina was
102 used immediately, while the other was stored for less than 2 h as an eyecup until use

103   (Figure S1). Only one of two retinas was used for the cone recordings from *Gnat1*^{-/-} retinas,

104   because the response appeared to become slow after the storage (Figure S5).

105   The retina was put on a filter paper attached on the top of a dome in the retina holder

106   (Figure S3A) (4). For a better adhesion between the filter paper and the retina, the surface

107   of the paper was cleaned in advance by gently pressing with Kimwipes. The retina was kept

108   under perfusion for 30 min to stabilize the system and then used for recordings.

109   The photoresponse, namely the transretinal voltage signal, was amplified 100 times

110   and low-pass filtered at 300 Hz in a differential amplifier (DP-311; Warner Instruments,

111   Holliston, MA, USA). The amplified signal was recorded at 1 kHz in a computer using a

112   digitizer (PL3504P; ADInstruments) and Labchart Pro 8.

113   The integration time was obtained by integrating the normalized response amplitude

114   over time (5). Because the normalized amplitude is dimensionless, the unit of the

115   integration time is ms.
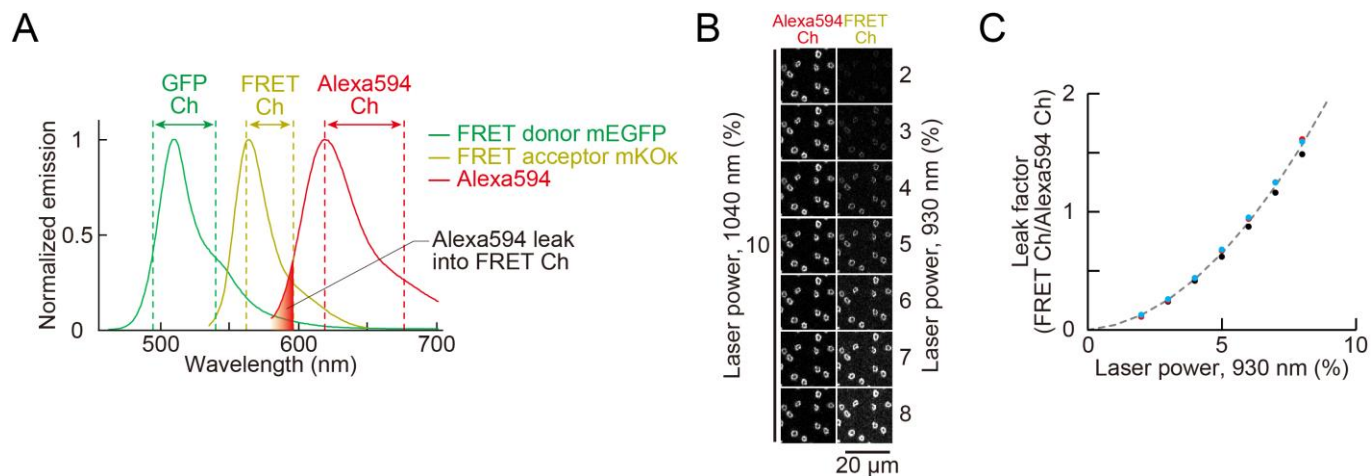
116

117   **Figure S1 to S5**
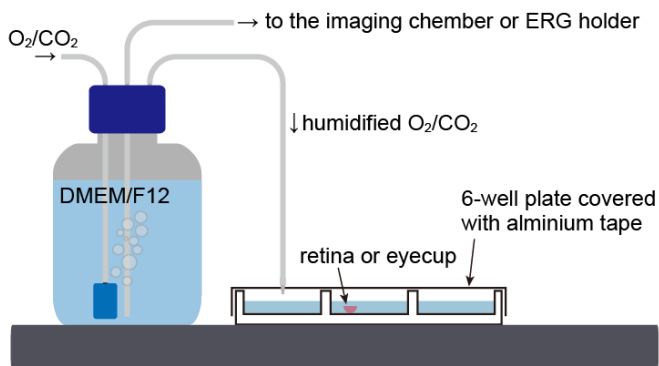
118

119   **Figure S1** Sample storage device. Humidity and medium pH were maintained by

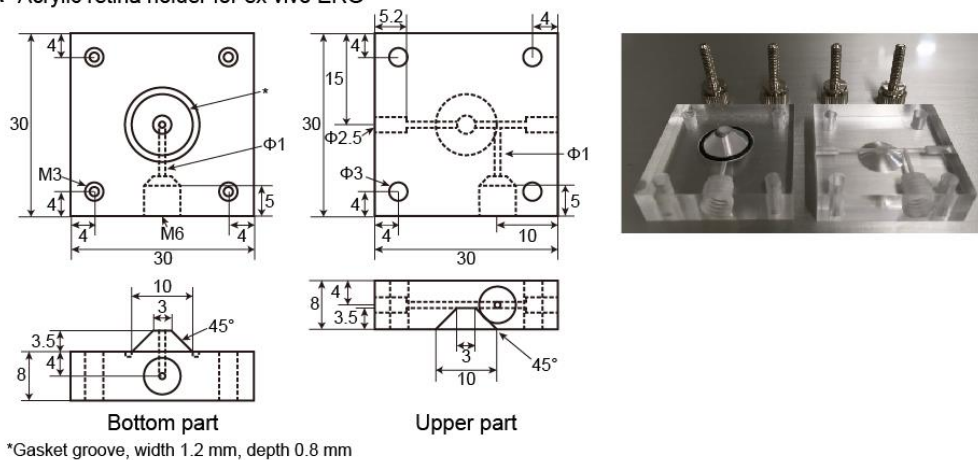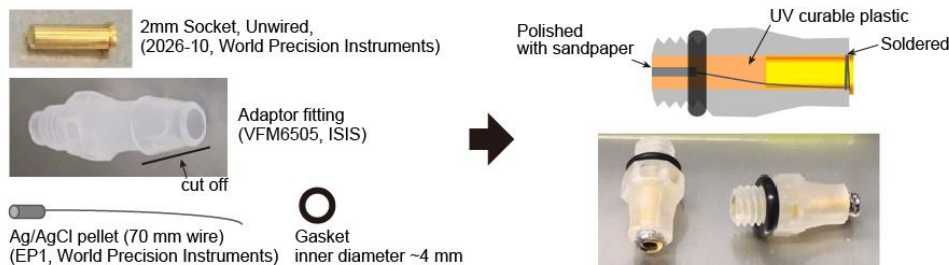120   delivering a gas mixture collected from the perfusion bottle.

121

Figure S2 Estimation of the leak intensity of Alexa594 into the FRET Ch. (A) Emission
spectra and detection range of the three channels used in Figure 3D. Emission spectrum
data were obtained from the FPbase ((https://www.fpbase.org/). (B) PNA-Alexa594 signal
imaged at the PRS in the non-fluorescent wild type B6J retina. (C) The ratio of Alexa594
intensities between the FRET Ch and Alexa594 Ch, plotted as a function of the 930 nm
laser power. n = 3 measurements from one retina. Plots were fitted with a quadratic
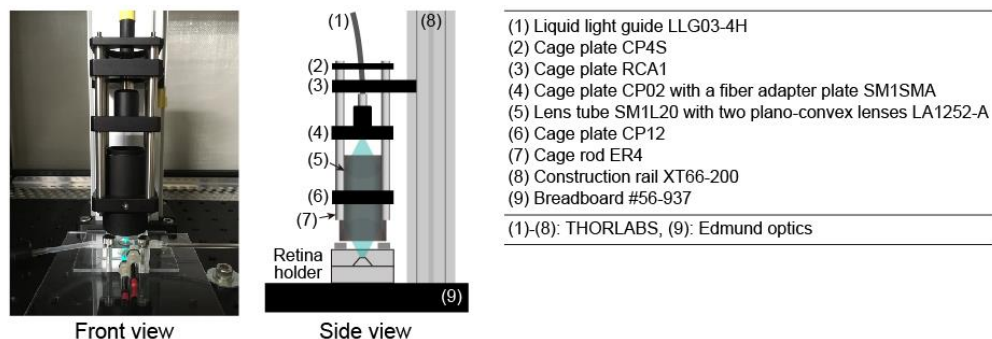function, and the curve was used to subtract the leak in Figure 3D.

129

A Acrylic retina holder for ex vivo ERG

Bottom part   Upper part

*Gasket groove, width 1.2 mm, depth 0.8 mm

B Electrode

2mm Socket, Unwired, (2026-10, World Precision Instruments)

Adaptor fitting (VFM6505, ISIS)

cut off

Ag/AgCl pellet (70 mm wire) (EP1, World Precision Instruments)

Gasket inner diameter ~4 mm

Polished with sandpaper

UV curable plastic

Soldered

C Optics to project a 3 mm light spot on the retina

Front view   Side view

Retina holder

(1) Liquid light guide LLG03-4H
(2) Cage plate CP4S
(3) Cage plate RCA1
(4) Cage plate CP02 with a fiber adapter plate SM1SMA
(5) Lens tube SM1L20 with two plano-convex lenses LA1252-A
(6) Cage plate CP12
(7) Cage rod ER4
(8) Construction rail XT66-200
(9) Breadboard #56-937

(1)-(8): THORLABS, (9): Edmund optics

130

131   **Figure S3** Devices used in *ex vivo* ERG recordings. (A) Design drawings and a picture of

132   the acrylic retina holder. M3 and M6 are screw holes 3 mm and 6 mm in diameter,

133   respectively. Both ends of the perfusion path were enlarged to fit with plastic connectors at

134   the ends of the silicon tubing. For further details, please see the previously published video

135   (4). (B) Materials for the electrode and the assembly. (C) Optics for the light stimulation

136   system assembled within the 30 mm cage system. The retina holder was fixed in position

137   with a concave acryl plate on the breadboard.

8

hyBRET-AMPK   CRALBP   Merged

GCL

IPL

INL

40 µm
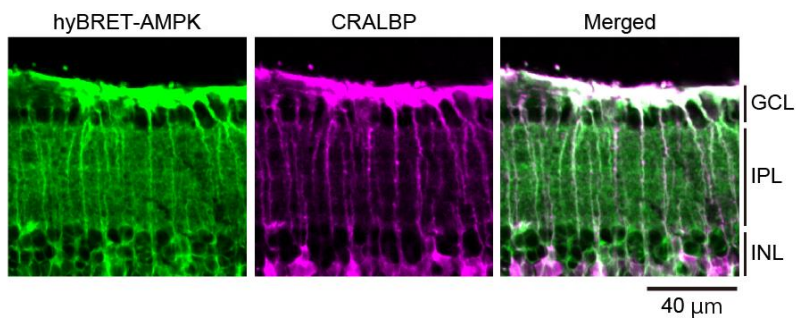
138

139   **Figure S4** Immunohistochemical identification of highly fluorescent cells in the hyBRET-

140   AMPK retina. Images were obtained from a fixed section of the hyBRET-AMPK retina

141   using a confocal microscope. The section was incubated with the CRALBP antibody to

142   label Müller cells. The green signal shows intrinsic fluorescence from the hyBRET-AMPK

143   biosensor, which was obtained by averaging signals from the 460–500 nm CFP channel and

144   520–560 nm YFP channel. CRALBP signals were detected with a 655–755 nm Alexa647

145   channel.

146

147
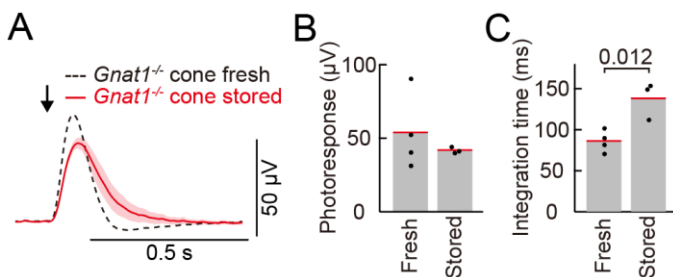
148

149   **Figure S5** Response slowdown in *Gnat1$^{-/-}$* cones after the storage. (A) Comparison of dim

150   flash responses recorded from the fresh and stored retinas. Recordings from the stored

151   retina (red) were performed after a 2 h incubation at room temperature in the sample

152   storage device (Figure S1). Mean ± SD, n = 3 retinas. The response of a fresh retina

153   (dashed curve) is shown for comparison. Mean of 5 retinas. Responses were elicited with a

154   2 ms, 500 nm, and 1000 photons µm^{-2} flash. (B and C) Photoresponse amplitude (B) and

155   integration time (C) of the response from fresh and stored retinas. Gray bars with red lines

156   show mean values. Values on the bars are P-values for the unpaired two-tailed t-test.

157   Significant difference was not detected in (B) (P >0.05).

9

158   **Supplemental References**

159   1.   Yamamoto, M., Kim, M., Imai, H., Itakura, Y., and Ohtsuki, G. (2019) Microglia-
160   Triggered Plasticity of Intrinsic Excitability Modulates Psychomotor Behaviors in
161   Acute Cerebellar Inflammation. *Cell Rep* **28**, 2923-2938
162   2.   Sato, S., Yamashita, T., and Matsuda, M. (2020) Rhodopsin-mediated light-off-
163   induced protein kinase A activation in mouse rod photoreceptor cells. *Proc Natl*
164   *Acad Sci U S A* **117**, 26996-27003
165   3.   Vinberg, F., Kolesnikov, A. V., and Kefalov, V. J. (2014) Ex vivo ERG analysis of
166   photoreceptors using an in vivo ERG system. *Vision Res* **101**, 108-117
167   4.   Vinberg, F., and Kefalov, V. (2015) Simultaneous ex vivo functional testing of two
168   retinas by in vivo electroretinogram system. *J Vis Exp*, e52855
169   5.   Baylor, D. A., and Hodgkin, A. L. (1973) Detection and resolution of visual stimuli
170   by turtle photoreceptors. *J Physiol* **234**, 163-198

171